Gold Nanostar Characterization by Nanoparticle Tracking Analysis

Natasha T. Le, Timothy J. M. Boskovic, Marco M. Allard, Kevin E. Nick, So Ran Kwon, and Christopher C. Perry*

Read Online

ACCESS | 📊 Metrics & More | 📖 Article Recommendations | 🔒 Supporting Information

ABSTRACT: We demonstrate the application of nanoparticle tracking analysis (NTA) for the quantitative characterization of gold nanostars (GNSs). GNSs were synthesized by the seed-mediated growth method using triblock copolymer (TBP) gold nanoparticles (GNPs). These GNPs ($\approx$ 10 nm) were synthesized from Au^{3+} ($\approx$ 1 mM) in aqueous F127 (w/v 5%) containing the co-reductant ascorbic acid ($\approx$ 2 mM). The GNS tip-to-core aspect ratio (AR) decreased when higher concentrations of GNPs were added to the growth solution. The AR dependency of GNSs on Au^{3+}/Au(seed) concentration ratio implies that growth is partly under kinetic control. NTA measured GNS sizes, concentrations, and relative scattering intensities. Molar absorption coefficients $\sim 10^9-10^{10}$ M^{-1} cm^{-1} ($\varepsilon_{400 \text{ nm}}$) for each batch of GNSs were determined using the combination of extinction spectra and NTA concentrations for heterogeneous samples. NTA in combination with UV−vis was used to derive the linear relationships: (1) hydrodynamic size versus localized surface plasmon peak maxima; (2) $\varepsilon_{400 \text{ nm}}$ versus localized surface plasmon peak maxima; (3) $\varepsilon_{400 \text{ nm}}$ versus hydrodynamic size. NTA for quantitative characterization of anisotropic nanoparticles could lead to future applications, including heterogeneous colloidal catalysis.
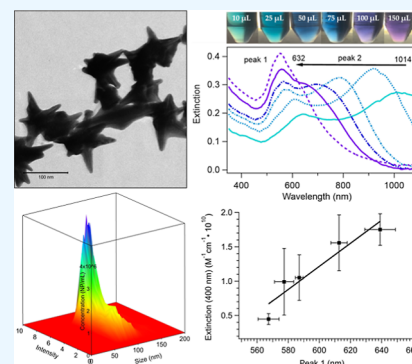
INTRODUCTION

Gold nanostars (GNSs) attract intense interest because of their exciting applications in molecular detection, imaging, catalysis, and therapeutics.[1−4] Incident light induces localized surface plasmon resonance (LSPR) in GNSs, with red shifting to the near-infrared range. The LSPR absorbance of GNSs in the infrared region allows soft tissue imaging. Light−matter interactions with GNSs are strong, causing huge enhancements in normalized local electric field intensities ($\sim 10^3-10^5$ fold), which are helpful for surface-enhanced Raman spectroscopy (SERS) applications.[5,6] The growing interest in GNSs is based on observations that nanomaterials' sizes and shapes affect their physical and chemical properties. Morphological control is achieved routinely for polyhedral gold nanoparticles (GNPs) in the $\sim 2-100$ nm range,[7,8] but this has not been the case for GNSs. Therefore, efforts are ongoing to achieve: (i) a mechanistic understanding of the GNS growth processes; (ii) develop shape control; and (iii) robust methodologies for conveniently calculating concentrations of colloidal suspensions for therapeutic applications.

To accurately quantify GNP concentrations, the standard protocol involves initial digestion in concentrated acid, followed by emission spectroscopy to measure total gold concentration. The NP concentrations are then calculated assuming polyhedral (quasi-spherical) shapes and homogeneous sizes. However, using this approach results in low quantitative accuracy for anisotropic NPs. Alternative rapid and nondestructive quantitative methods are needed. Quantification of size and concentration of GNSs is challenging due

to their heterogeneous nature. Nanoparticle tracking analysis (NTA) can visually track and count NPs within the 30−1000 nm range and estimate their concentrations.[9] NTA has been used to determine the sizes and concentrations of vesicles and gold nanomaterials.[10−13] However, it is noted that the recorded sizes represent hydrodynamic diameters and, for anisotropic nanoparticles (NPs), are equal to an equivalent sphere with some translational diffusion coefficient. The typical rotational frequency of gold nanorods is 10^3 s^{-1}, while the NTA camera collection time is 10^2 s^{-1}, and thus NP anisotropy is averaged out in the extracted hydrodynamic diameter.[14] The concentration determined from NTA and the extinction spectra from UV−vis spectroscopy are used to determine the extinction coefficient. NTA accounts for heterogeneity in each unique GNS batch solution.

GNS synthesis protocols are classified into seeded and one-pot approaches.[3] Seed-mediated syntheses are based on temporal separation of nucleation and growth processes.[8] The most common method for synthesis of GNSs is based on the protocol used to make gold nanorods.[15,16] In this context, single or polycrystalline GNP seeds are added to a growth solution containing precursor gold salt, a cationic surfactant
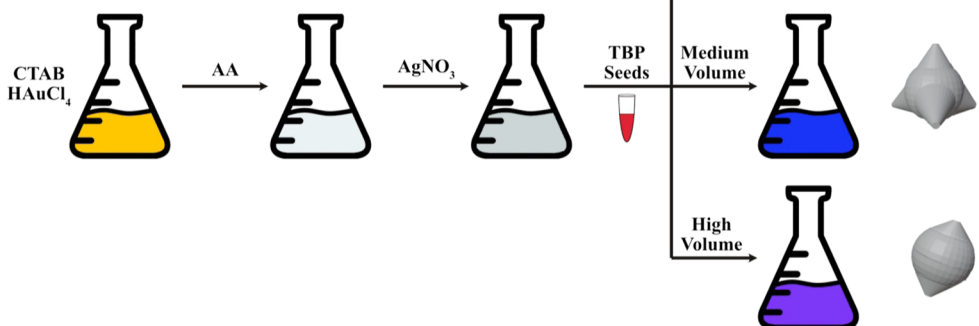
Figure 1. Steps in the seed-mediated growth of GNSs from F127 TBP-coated GNP seeds. The Au^{3+}/Au(seed) ratio determines the tip-to-core aspect ratio, if other parameters of temperature and reagent concentrations [AA, $AgNO_3$] remain fixed. Increasing the Au^{3+}/Au(seed) ratio, when the seed concentration is low, increases the tip-to-core aspect ratio. CTAB: cetyltrimethylammonium bromide.

such as cetyltrimethylammonium bromide (CTAB), and a weak reducing agent [ascorbic acid (AA)].[17−20] Alternatively, one-step GNS synthesis approaches include using Good's buffers, such as N-2-hydroxyethylpiperazine-N′-2-ethanesulfonic acid (HEPES), as both a reducing and stabilizing agent.[21−25]

The size and crystallinity of GNP seeds dictate the final morphology of GNSs.[26−28] In growth solutions containing AA and CTAB, single-crystal GNP seeds (< 3 nm) produce rods, while polycrystalline seeds (> 5 nm) produce various morphologies including polycrystalline rods, bipyramids, plates, stars, and polyhedral NPs.[17,24] Moreover, various shapes (rods, dog-bones, plates, etc.) of GNPs can be produced when Pluronics are included as additives in the growth solution.[29] For example, Nehl and co-workers used polymer-stabilized citrated NP seeds (≈ 10 nm) in a growth solution to produce GNSs.[30] However, the authors noted that, while commercially produced citrate seeds lead to very reproducible results (∼ 14% yield of three or more tips), they were wary of ultimately relying on a commercial supplier of seed particles.

Bipyramidal structures are observed using CTAB[31]- or CTAC[32]-coated GNP seeds. In the seedless one-pot approach, the morphology of the multi-spiked NPs is penta-twinned.[19] These produced penta-twinned structures exhibit growth along the ⟨110⟩ direction. The reducing power of AA (redox potential more negative) increases with pH, with a larger fraction of (partially) deprotonated AA present, which leads to higher reduction rates.[32] Mass transport of gold adds to multiple surface planes where reduction occurs both generally and at the interfacial regions. If temperature and reagent concentrations (Ag^+, AA) are controlled, then the Au^{3+}/Au(seed) ratio determines the GNS tip-to-core aspect ratio (AR).[33−37] Increasing the Au^{3+}/Au(seed) ratio increases the AR because there is more gold per NP.[35] Similarly, in addition

to influencing the tip-to-core AR ratio, silver can stabilize the spikes on GNSs.[36]

GNS growth conditions can be adjusted so that either the thermodynamic or kinetic products predominate. NP growth is under thermodynamic control if the lowest energy structures are formed. In this context, the diffusion rate (V_{diff}) of adsorbed atoms is rapid, with the system in equilibrium between high and low energy planes. However, to a lesser extent, the process may also be subject to the lowest energy barrier pathway (lowest transition energy) and kinetic control.[38] With kinetically controlled growth, the predominant shape is determined by the rate of deposition (V_{dep}) to exposed high-energy facets.

The balance between kinetically and thermodynamically controlled growth is expressed as the ratio between gold atom deposition rate and diffusion rate (V_{dep}/V_{diff}).[39,40] When $V_{dep}/V_{diff} < 1$, $V_{diff} > V_{dep}$, the depositing atoms diffuse to corners and edges, resulting in isotropic growth to polyhedral shapes, and NP growth is thermodynamically controlled. Regulation of V_{diff} can be adjusted by increasing temperature or using different capping agents, such as silver or polymer, with selective binding to high-energy planes. When $V_{dep}/V_{diff} > 1$, $V_{dep} > V_{diff}$; the surface diffusion activation barrier is sufficiently high so that atoms deposited on the highest-energy surfaces undergo negligible diffusion. Therefore, the NP growth becomes kinetically controlled, which facilitates anisotropic NP growth. Deposition rate, V_{dep}, is positively associated with the reaction rate, which can be increased by using a lower concentration of seeds or increasing the reductant's strength.

From kinetic and thermodynamic considerations, the GNS branching depends on the magnitudes of V_{dep} and V_{diff}.[37] High values of V_{dep} represent adatoms in the growth solution adsorbing on seed planes with high surface-free energies. With high values of V_{diff} adsorbed adatoms diffuse rapidly between high- and low-energy planes, and equilibrium is established. A partial explanation for anisotropic growth includes the

competition between the rate of Au mass transport (proportional to V_{dep}) to the high energy sites and adatom diffusion rates (V_{diff}) between faces. Here, V_{dep} is slightly larger than V_{diff} ($V_{dep} \sim V_{diff}$). Moreover, this V_{dep}/V_{diff} ratio is altered by adjusting the concentration of seeds or the reduction rate of Au^{3+}.[37] Assuming that GNS growth is reaction-limited for each temperature, V_{dep} is proportional to the $Au^{3+}/Au(seed)$ ratio. In our experiments, increasing seed concentration reduces the tip-to-core ratio, with fewer spikes and larger cores due to fewer depositing gold atoms per NP. The observed spike growth of fivefold symmetry was also present in a high-yield-seeded protocol using triton-X as a surfactant.[36] Thus, by manipulating V_{dep}, we can adjust ARs.

In this work, the GNS ARs were adjusted by varying the concentration of GNP seeds added to the growth solution. The silver concentration (50 μM) was high enough to inhibit surface gold adatom diffusion, as confirmed by the stability of UV−vis LSPR peaks days after the end of the reaction. Novel use of triblock copolymer (TBP) Pluronics-coated GNP seeds was employed to synthesize GNSs (Figure 1). TBPs are blocks of polyethylene oxide (PEO) and polypropylene oxide (PPO) in the form $PEO_x-PPO_y-PEO_x$, which can be used as reducing and stabilizing agents during synthesis of GNPs. This is a simple, robust, and environmentally benign protocol to synthesize GNPs. Indeed, citrated GNPs have already been used as seeds in GNS synthesis.[41−43] However, in contrast to the Turkevich method, the compromise of broader TBP GNP size distributions is offset by its robust synthesis at room temperature. We note that capping of citrated GNPs by polyvinylpyrrolidone (PVP) has been employed successfully for seeds used to synthesize GNSs from $HAuCl_4$ in DMF.[35] However, this requires 24 h activation in the PVP solution. We hypothesize that (a) F127 TBP micellar cavities are soft templates imparting size control and (b) any presence of co-reductants increases the nucleation rate, resulting in smaller NPs. Hence, AA was added to the F127 solution to reduce Au^{3+} to Au^+. TBP-coated GNP seeds ($\sim$ 10 nm) of varying concentrations were then added to a precursor solution for robust yields of GNSs. The growth solution was supplemented with AA as a weak reductant, while other reagents (CTAB, silver nitrate) passivate the surface and allow for reproducible shape control. Furthermore, by adjusting the added seed volume, we can adjust GNS ARs. The visualization and quantification capabilities of NTA were used to determine sizes, concentrations, and molar absorption coefficients of GNSs.

■ MATERIALS AND METHODS

Materials. Ammonium hydroxide (28−30%), NaOH ($\geq$ 98%), silver nitrate ($\geq$ 99%), gold(III) chloride hydrate ($HAuCl_4 \cdot xH_2O$; 99.9% trace metals basis), Pluronic F127 TBP of ethylene oxide (EO), propylene oxide (PO) ($EO_{100}PO_{65}EO_{100}$, MW $\approx$ 12500; lot no. BCBT6374), CTAB (99%), AA (reagent grade), sodium borohydride ($\geq$ 98%), citric acid ($\geq$ 98%), disodium citrate ($\geq$ 98%), 3-aminopropyltriethoxy silane (APTES) ($\geq$ 98%), triethanolamine ($\geq$ 98%), glutathione ($\geq$ 98%), 4-nitrophenol (4-NP) ($\geq$ 98%), 4-nitrothiophenol (4-NTP) ($\geq$ 98%), poly(ethylene glycol) methyl ether thiol ($PEG_{6k}SH$) (MW $\approx$ 6000; lot no. MKCL 4582), and 3-(N-morpholino) propanesulfonic acid (MOPS) were used as received (Sigma-Aldrich, Milwaukee, WI, USA). Milli-Q deionized (DI) water (18.2 MΩ cm) was used.

Instrumentation. UV−vis spectra were recorded using either Varian Cary 300 (Agilent) (400−900 nm) spectrophotometer or StellarNet (StellarNet Inc, Florida) (200−1080 nm) systems.

Atomic force microscopy (AFM) measurements were collected using the amplitude-modulated (peak force tapping) mode of a multimode-8 AFM instrument (Bruker, Santa Barbara, CA). Digital transmission electron microscopy (TEM) was done with a Thermo Scientific Talos L120C (Experimental details in Supporting Information). Crystal sizes of seeds and stars were determined with powder X-ray diffraction (XRD), using a Bruker D8 ADVANCE with a Lynx-Eye strip detector. The seeds and stars were prepared and then washed with water to remove polymers (Experimental details in Supporting Information).

Dynamic Light Scattering and Nanoparticle Tracking Analysis. NP sizes, charges, and concentrations were also measured by light scattering. Dynamic light scattering (DLS) and zeta potential (ZP) measurements were made using a model Z3000 (Nicomp, Port Richey, FL) size analyzer. The cylindrical sample (500 μL) was laser-illuminated (632 nm), and the scattered light was collected at 90°.

Additionally, GNS sizes were quantified (500 μL aliquot, 100-fold diluted) by NTA using a model NS3000 instrument (NanoSight, Malvern Panalytical, CA). NTA can simultaneously measure the GNS concentration, scattering intensity, and hydrodynamic diameter. The advantage of the NTA technique is that it is not biased toward larger NPs or aggregates. Microscope video capture (640 × 480 pixels, 30 frames per second) records the scattered light from individual particles. Size estimates (3−1000 nm) are derived from each particle's Brownian motion based on the Stokes−Einstein equation using proprietary software. Equation 1 measures the mean squared displacement $\overline{(x, y)^2}$ of the NP in two dimensions.[9]

$$\overline{(x, y)^2} = \frac{2k_B T}{3R_H \pi \eta} \tag{1}$$

The rate of NP movement is dependent on the temperature of the solution T, solution viscosity η, and hydrodynamic radius, R_H, where k_B is the Boltzmann constant. NTA of the relative scattering intensities as a function of the refractive index can distinguish NPs of comparable diameters.

Determination of Molar Absorption Coefficients. GNS molar absorption coefficients were calculated using Beer's law: $\varepsilon = A/(C \cdot 1 \text{ cm})$, where A is absorbance from the UV−vis spectra and C is the GNS concentration (NP/mL), which is converted to mol L^{-1}. GNSs were diluted (10−500-fold) with DI water prior to injection into the flow cell of the NTA instrument. An average of five runs for each sample was used to determine concentrations, sizes, and intensities. Three relationships are formed where size (nm), molar absorption ε(M^{-1} cm^{-1}), wavelength λ (nm), and B, C (nm), D (nm^{-1}), E, F (nm^{-1}), and G are constants.

$$\text{size} = B \cdot \lambda + C \tag{2}$$

$$\varepsilon_{400} = 10^{10} \cdot M^{-1} cm^{-1}(D \cdot \text{size} + E) \tag{3}$$

$$\varepsilon_{400} = 10^{10} \cdot M^{-1} cm^{-1}(F \cdot \lambda + G) \tag{4}$$

Thus, from these calculated molar absorption coefficients, the concentration (μg mL^{-1}) of gold atoms in solution can be
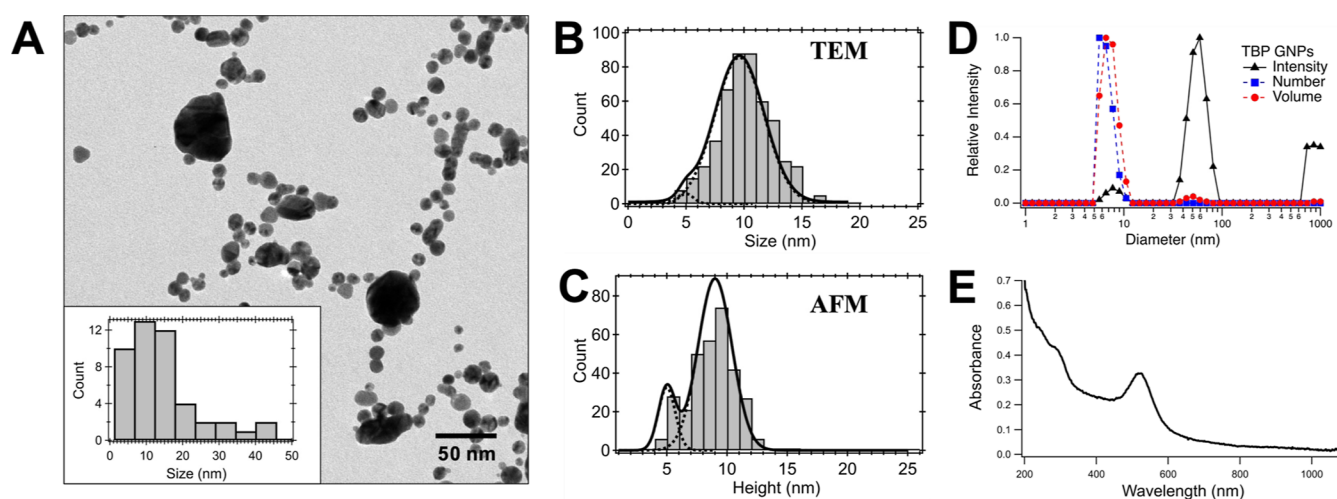
Figure 2. Microscopy characterization of F127 TBP-coated GNPs. These seeds are synthesized using 5% w/v F127 in 1 mM MOPS buffer at ≈ 35 °C. (A) TEM images of GNPs (scale bar 50 nm). Inset: Full size distribution of (A). (B) TEM size distribution, for particles < 25 nm, with Gaussian peak fit maxima at 5.0 ± 0.9 and 9.6 ± 3.0 nm (N = 490). (C) AFM size distribution, for particles < 25 nm, with Gaussian peak fit maxima at 5.0 ± 1.0 and 9.0 ± 2.0 nm (N = 315). (D) DLS intensity-volume-number-weighted distributions. (E) UV−vis of TBP-coated GNPs.

determined according to the equation below, where C_{Au} is the concentration of gold ($\mu g\ mL^{-1}$), A_{400} is the absorbance at 400 nm, M_{Au} is the molecular weight of gold (FW: 196.97 g mol^{-1}), ε_{400} is the molar absorption coefficient ($M^{-1}\ cm^{-1}$) at 400 nm, and l (cm) is the optical path length.

$$C_{Au} = 10^3 \times \frac{A_{400}M_{Au}}{\varepsilon_{400}l} \tag{5}$$

TBP Seed Synthesis. Before use, all stock solutions were immersed in Lab Armor Beads and equilibrated at 25−37 °C for 30 min. Solutions of 1−5% w/v F127 were prepared at pH ∼ 5−8 in citrate (pH ≈ 5−6) or MOPS (pH ≈ 7−8) buffers (1 mM final). In a typical NP synthesis, 5% w/v F127 in buffer (10 mL, 1 mM) was made by combining 10% w/v F127 TBP (5 mL), water (4 mL), and buffer (1 mL, 10 mM stock). Then, solutions of AA (200 μL, 0.1 M) followed by HAuCl$_4$ (100 μL, 0.1 M) were added, followed by vigorous shaking. Formation of GNPs was left to continue for 30 min at temperatures between 25 and 37 °C. Citrated GNPs were synthesized as previously described.[44] To these GNPs, F127 was added to give 5% w/v F127. Growth experiments were performed with unwashed and washed (16,000 ×g, 20 min) GNPs.

GNS Synthesis. All stock solutions were equilibrated at ≈ 35−37 °C for 30 min before use. Two stock solutions were prepared: (**A**) CTAB (0.1 M) and (**B**) HAuCl$_4$ in CTAB (100 μL, 0.1 M Au^{3+} in 10 mL, 0.1 M CTAB). L-AA (100 μL, 0.1 M) was added to 5 mL of solution **A**. To this solution was added 5 mL solution **B**. Next, AgNO$_3$ (100 μL, 5 mM) was added and the solution vortexed for ∼ 5 s. GNS growth was started within 1 min by adding TBP seed solution (10−150 μL), followed by vigorous shaking. GNSs were left to form at ≈ 35−37 °C for a minimum of 30 min.

Functionalization of GNSs. GNSs were functionalized by PEG as previously described.[45] GNSs (1 mL) were washed twice (5 min, 10,000 ×g, suspended in 5% w/v F127 to passivate the microcentrifuge tubes) and suspended in 1 mL 50:50 v/v Tris−HCl:5% F127 (pH 3) solution. PEG$_{6k}$SH (5 μL, 1 mg mL^{-1}) was then added. The solution was sonicated for 30 min, centrifuged twice (5 min, 10,000 ×g, suspended in

5% w/v F127 to passivate the microcentrifuge tubes), and suspended in water.

■ RESULTS AND DISCUSSION

Protocol for GNS Synthesis and Characterization. The synthesis of GNSs follows the seed-mediated approach with TBP-coated GNPs used as seeds (Figure 1). Advantages of using polymer coated rather than citrated seeds include rapid GNP generation at room temperature, robustness, cost-effectiveness, and higher stable GNP concentration.[46] We produced GNP seeds from a precursor solution containing 5% w/v F127 and AA (2 mM) by adding HAuCl$_4$ (1 mM). Control of pH is necessary to ensure smaller (∼ 10 nm) GNP sizes. The solution is buffered using citrate (pH ∼ 6) or MOPS (pH ∼ 7) before adding gold salt. Because AuCl$_4^-$ has a pK_a of 3.3, the speciation of gold is dominated by AuCl$_3$(OH)$^-$ (pK_a ≈ 6.2). These GNPs are added to a growth solution at ≈ 35−37 °C containing CTAB, AA, and gold and silver salts. The sizes and shapes of GNSs are adjusted by varying the volume of added GNP seeds.

GNP Synthesis Using Co-Reductants F127 and AA. GNP shapes and sizes are controlled by varying the TBP to gold salt ratio, TBP/Au^{3+}.[47,48] It is hypothesized that the reduction of Au^{3+} proceeds via the oxidation of EO groups in a pseudo-crown ether complex with gold salts, so that the reduction of Au^{3+} follows the sequence Au^{3+} → Au^{2+} → Au$^+$ → Au$^\circ$.[49−51] For size control and increased reduction rates, AA is also added to the F127 solution as a co-reductant. The rate-determining step is the reduction of Au$^+$ ions,[49] which can migrate into micellar cavities resulting in disproportionation [3Au$^+$ ⇆ 2Au$^\circ$ + Au^{3+}],[51] followed by metal atom coalescence forming Au nanoclusters to yield primary nanocrystallites. Pluronic F127 reduces Au^{3+}, caps the GNPs, and produces a heterogeneous size distribution.

Representative microscopy images of GNP seeds show multiple populations (Figures 2A). Size distribution analysis by TEM and AFM indicates bimodal size distributions centered around 5 and 10 nm and interspersed with larger aggregates of ∼ 50 nm (Figure 2B,C). Sizes are confirmed by DLS showing two populations centered at ∼ 10 and ∼ 50 nm (Figure 2D). For TBP-coated GNPs, the UV−vis LSPR maximum is ≈ 520

nm (Figure 2E). From the UV–vis spectrum, we can estimate GNP size and concentration. The concentration of GNPs was ≈ 25–30 nM, estimated from UV–vis spectra using absorbance ratios $\left(R = \frac{A_{520}}{A_{450}}\right)$.[52] Moreover, the 520 nm LPSR peak absorbance against time follows autocatalytic growth,[47,48] after a brief induction period (not shown). GNP growth is essentially complete after 30 s.

To evaluate the effect of temperature on NP size, syntheses were performed between 25 and 37 °C in 5% w/v F127 solutions buffered with citrate or MOPS (1 mM). Representative DLS data in MOPS buffer show primary populations of GNPs below 10 nm with larger aggregates above 30 nm (Supporting Information Figure S3A–D). Increasing the temperature shifts the sizes of the dominant population from ≈ 5 to ≈ 10 nm. However, increasing the buffering capacity (2 mM) removes this temperature dependence and the dominant size population remains ≈ 5 nm. The temperature dependence of seed size is confirmed by the UV–vis absorbance increase at 400 nm when temperature is increased from 30 to 37 °C (Supporting Information Figure S3E–F). GNPs synthesized in citrate-buffered solutions are smaller, as demonstrated by their lower absorbance at 400 nm. The impact of buffering was examined on the 5% w/v F127 micelle size and on the role of micellar cavities as templates for NP growth (Supporting Information Figure S4). The average micelle size is ≈ 3 nm in both buffers, implying that buffering does not affect micellar size. However, pH affects Au^{3+} speciation and AA redox potential, which determine reduction rates and subsequent GNP sizes. Moreover, the bimodal population distribution and low-resolution TEM images of multiple morphologies include penta- and hexa-twinned and truncated hexagonal shape characteristic of polycrystalline NPs (Supporting Information Figure S5).

GNS Preparation. Reproducible synthesis of high-yielding GNSs was achieved by controlling seed crystallinity and concentration, pH, AA concentration, $AgNO_3$ concentration, type of surface coating, and temperature. The growth solution contains Au^+, and we can assume that Au^+ ions become reduced as they bind the F127-coated GNPs.[32] Indeed, examination of the morphology of the TBP-coated GNP seeds shows mixtures of plate, icosahedral, and decahedral morphologies indicative of penta-twinned multiple twinned structures (Supporting Information Figure S5). Decahedral structures have exclusive {111} facets. Icosahedral morphologies have both {111} and {100} facets.[53] The morphologies of multiple twinned seeds are the platform for the generation of branched NPs. CTAB binding would be expected to follow the trend in surface free energies {110} > {100} > {111}. Indeed, calculated adsorption energies of CTA^+Br^- are higher on {110} and {100} than {111} facets.[37] Based upon these thermodynamic arguments, growth would be preferred in ⟨111⟩, but hindered in ⟨110⟩ directions. However, twin boundaries of high strain energy in TBP seeds between {111} planes are active sites for secondary growth.[36,53] This is manifested experimentally in the preferential growth along ⟨110⟩ and ⟨100⟩ directions[32,33,37] and is likely in our case.

GNS growth conditions were adjusted, so kinetic products predominate. Kinetic control is achieved by having the rate of deposition (V_{dep}) larger than the diffusion rate (V_{diff}). With kinetically controlled growth, the predominant shape is determined by the rate of deposition (V_{dep}) to exposed high-energy facets. In contrast, with NP growth under thermody-namic control, the diffusion rate (V_{diff}) of adsorbed atoms is rapid. Here, the system is in equilibrium between high- and low-energy planes. However, under our experimental conditions, kinetic control was achieved by adjusting the Au^{3+}/Au(seed) ratio.

Figure 3A–D demonstrates that the length of spikes relative to cores decrease with higher GNP seed concentration (on a
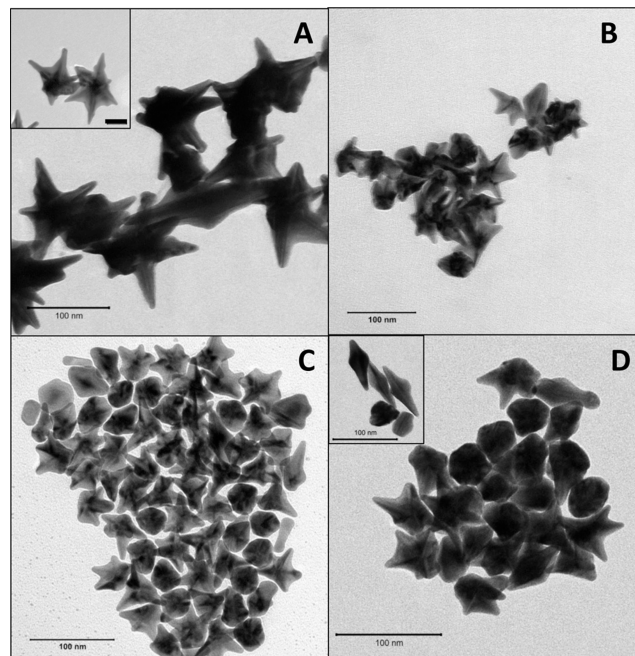

Figure 3. GNSs made using F127-coated GNP seeds. TEM images of GNSs (10 mL scale) seeded with (A) 10, (B) 50, (C) 100, and (D) 150 μL of F127-coated GNPs. Scale bar of (A) inset is 50 nm. All other scale bars are 100 nm.

10 mL scale). Inset images (A,D) show fivefold penta-twinned and nanobipyramidal morphologies. Size distributions from TEM are likely underestimated due to projections of three-dimensional structures onto a two-dimensional surface. Despite these limitations, we estimated the number and length of spikes relative to the core. Spike lengths decrease when higher volumes of added seeds are used (C,D). For GNSs produced with 10 μL seeding solution, four or more spikes of 30–60 nm are observed with core sizes of ≈ 50 nm. In contrast, when 150 μL seeding solution is used, the average number of observed spikes tends to be fewer than four, with frequent presence of nanobipyramids. Further, the spike lengths are reduced to ≈ 30 nm and core sizes are ≈ 25 nm.

GNSs prepared using monodispersed citrated seeds, which had also been coated with F127, were observed with similar size distributions (DLS), lack of control on AR, and an undefined number of spikes (TEM) (Supporting Information Figure S6A–C). As a result, GNS yields above 40% were achieved. However, two types of GNP seeds were tested. Seeds A: Monodispersed GNP seeds (∼ 10 nm), made by Turkevich method, were then suspended in 5% F127. Seeds B: In situ produced seeds were made by the co-reduction with AA and 5% F127. GNSs made from ∼ 12 nm type A seeds had sizes ∼150–200 nm, with typical core sizes ∼ 100 nm (Table S2). The density of GNS spikes was high, on average > 6. In contrast, GNSs synthesized with type B seeds had sizes of ∼ 100 nm, with typical core sizes of ∼ 50 nm. In this case, the
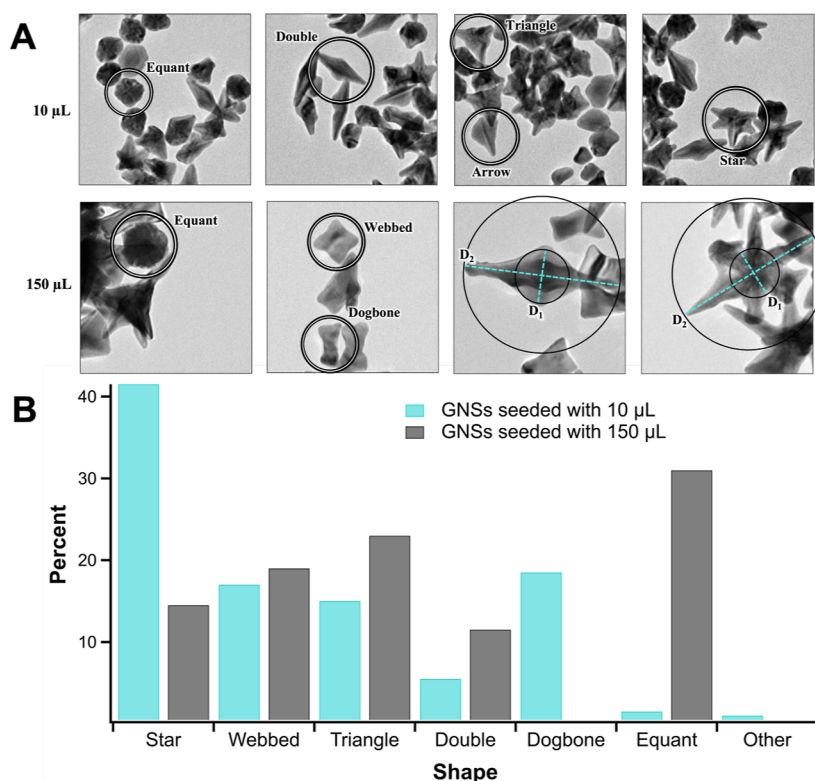
Figure 4. Distribution of shapes of 10 and 150 μL preparations. Shape assignments were based on the number of points and were unambiguously assignable for nearly all particles. Statistics are based on manual measurements of 200 particles. (A) TEM images of GNSs made using 10 μL (first row) and 150 μL (second row) of F127-coated GNP seeds. Diameter measurements made using a small inner circle that encloses the particle core and a larger circle that encloses the entire particle. (B) Graph showing distribution of shapes of GNSs made using 10 μL (blue bar) and 150 μL (gray bar) of F127-coated GNP seeds.

density of GNS spikes was lower, on average < 6. Although the GNS yield is lower ($\approx$ 40% vs $\approx$ 50%) using type B seeds, examination of TEM images indicates that the AR can be varied by adjusting the Au^{3+}/Au(seed) ratio.

GNS growth is partly under kinetic control and is expressed by the ratio between deposition (V_{dep}) and adsorbed adatom diffusion (V_{diff}) rates. If GNP growth rate is the same on all GNP facets, the yields and ARs would track the size distributions of the seeds. This is not the case because ligand-capping agents will have different binding energies depending on the facet where they are chemisorbed; V_{dep} will be facet-dependent. For example, citrate binds preferentially on Ag {111} facets, while PVP binds on {100} facets.[54] The strength and face specificity of ligand binding to GNP seeds determine GNS yields and ARs. For GNP seeds, we expect preferential facet chemisorption of F127, where F127 serves a dual role as a capping and reducing agent. The observation of spikes > 6 using polymer-stabilized citrated seeds suggests V_{dep} > V_{diff}. Hence, the growth is under kinetic control. In contrast, with the TBP seeds, $V_{dep} \sim V_{diff}$ because tuning the ARs by adjusting the Au^{3+}/Au(seed) ratio is possible. By changing the growth conditions, namely, ligand, pH, and temperature, we can alter the balance between thermodynamic and kinetic control.

Further quantitative TEM analysis of 200 NPs at 10 and 150 μL seed preparation shows heterogeneous (polydispersed) shapes and sizes. NPs were categorized into various shapes [star, webbed, triangle, double, dog-bone, equant (round), and other] based on the number of protruding points and their relative lengths and positions (Figure 4, Table S1). We

estimated the GNS ARs from TEM two-dimensional projections. The NP size is defined by two diameters: D_1, the circle within the NP core at the minimal boundary, and D_2, the smallest circle that encloses all extensions of the NP. Hence, AR is the ratio D_2/D_1. The average ARs are $\approx$ 2.2 $\pm$ 0.4 and $\approx$ 1.8 $\pm$ 0.2 for GNSs prepared with 10 and 150 μL, respectively.

Considering that the technical definition of a star is a core with spikes, the webbed, triangle, and double shapes could also be considered stars. In the 10 μL preparation, stars with $\geq$ 5 spikes account for 41% of the shapes with AR $\approx$ 2.5. Webbed, dog-bone, and arrowhead shape abundances (15−19%) are comparable. The dog-bone shape is abundant at 18.5%. The largest particles are doubly terminated but are only slightly larger than the stars. Webbed samples have thicker centers and projections with a thinner web of material between the points. In contrast, average NP sizes in each shape category after 150 μL seed preparation are smaller than their equivalent in the 10 μL preparation. Stars with $\geq$ 5 spikes account for $\approx$ 15%, with AR $\approx$ 2.0. The two most abundant particle shapes in the 150 μL preparation are equant (nearly spherical) and triangular or arrow shape, dominated by growth of one long pyramid. Bipyramidal NPs are largest in both preparations with ARs of $\approx$ 2.7.

TEM characterization illustrates the effect of seed crystallinity and pH on growth of GNSs (Supporting Information Figure S7C,D). When single-crystal seeds (< 3 nm) are made in situ by addition of $NaBH_4$, then gold nanorods with AR $\approx$ 3 are formed (Supporting Information Figure S7A,B). The AR can also be increased by lowering the

pH of the growth solution (via addition of 10 μL, 37% HCl). In contrast, GNSs are formed when using polycrystalline (> 5 nm) seeds. Lowering the pH of this growth solution (via addition of 10 μL, 37% HCl), however, does not lead to increased AR but to the production of polyhedral and nanobipyramidal shapes.

The reduction rates of the sequence $Au^{3+} \rightarrow Au^+ \rightarrow Au^0$ are pH-dependent. In the growth solution, the Au^{3+} to Au^+ reduction rate is not the rate-limiting step. However, the Au^+ reduction and nucleation are rate-limiting.[49] At low pH, AA is a weaker reducing agent, and a larger fraction is protonated, which leads to lower reduction rates.[55] Another possible contributing factor to $Au^+ \rightarrow Au^0$ reduction is pH modulation of the water solvation cage around adsorbed species (CTA^+Br^-, $Au^{+1/+3}$, AA) on the growing NP. This solvation cage causes a charge and concentration gradient, affecting the surface's mass transport. Molecular dynamics (MD) simulations suggest that CTAB is packed more densely on (110) and (100) faces, compared to the (111) face, while growing the single-crystal gold nanorod surfaces.[56] These simulations identified water−ion channels between adsorbed CTAB, which are wider on the (111) facets. The higher potential difference accumulation between the surface and the electrolytic solution on (111) planes was assigned to greater $AuCl_2^-$ diffusion to these surfaces. In practice, however, the actual diffusing species is likely $CTA\text{-}AuBr_2^-$, suggesting preferential gold nanorod growth along ⟨111⟩ directions because of weaker CTAB packing on {111} facets. Lowering the pH increases the concentration of hydronium species that will facilitate solvent reorganization around adsorbed CTAB molecules and widen water−ion channels. This will further enhance diffusion of the reactants toward {111} facets to increase anisotropic gold nanorod growth. Thus, the AA reduction rate (decrease) and surface solvation reorganization (larger channels) are competing contributions to V_{dep} at low pH.

In contrast to gold nanorods, the GNS preparation relies on the polycrystallinity of the NP seeds, which have predominant {100} and {111} facets. Consequently, the growing spikes correspond to individual rods growing from the core along ⟨110⟩ directions, where there is denser CTA^+Br^- packing on {111} facets. Based on this interpretation, lowering the pH of the GNS growth solutions would be expected to increase the width of water−ion channels on the NP core and spike {111} side facets allowing for faster Au adatom diffusion. Conversely, growth rates along ⟨110⟩ directions are reduced, and Au adatoms have increasing probability to deposit on all planes. Here, V_{diff} increases relative to V_{dep}, resulting in quasi-spherical NPs.

GNS Characterization by UV−Vis and XRD. Representative UV−vis spectra of GNSs, synthesized using increasing volumes of GNP seeds, have two LSPR bands of interest. These bands become blue-shifted and coalesce with increasing seed concentrations (Figure 5). This can be interpreted using plasmon hybrid theory as a form of energy coupling of in- and out-of-phase plasmon resonances.[57] Higher energy (shorter wavelength) and lower energy (longer wavelength) peaks represent core and spike LSPR resonances, respectively.[20,58] Core and spike morphologies of the GNSs, specifically the tip aperture angle and length, strongly affect the spike energy mode of the LSPR.[20,57] Additionally, tip numbers modulate the intensity of the lower energy band.[58] Core size, however, has a milder influence. The decrease in separation between peaks 1 and 2, associated with higher seed concentrations, is
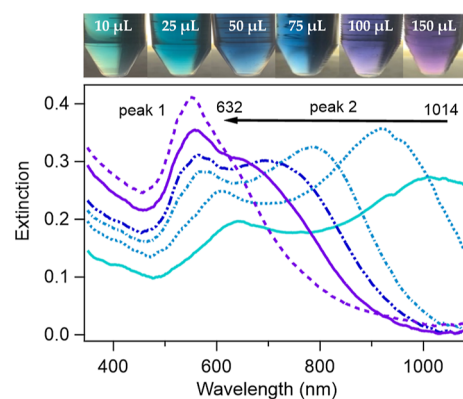

Figure 5. Representative UV−vis spectra of GNSs (1:10 dilution) grown using 10, 25, 50, 75, 100, and 150 μL GNP seeds.

attributable to the decreasing tip-to-core (diameter) AR, consistent with TEM observations. With 10 μL of GNP seed solution added, the GNS spikes (30−60 nm) are larger than the average core ($\sim$ 50 nm, AR $\sim$ 2.5). As a result, peak 2 in the UV−vis spectrum is at $\approx$ 1000 nm. In contrast, the AR is below 2, following use of 50 μL of seeds, because GNS tip lengths decrease to $\sim$ 20 nm while the core size remains $\sim$ 30 nm. With increasing seed concentrations, the wavelength of peak 2 decreases toward $\sim$ 600 nm.

The spectra in Supporting Information Figure S8B−E illustrate how the average ARs depend on the seeds. Supporting Information Figure S4A−D shows the DLS sizes of GNP seeds prepared under different buffer concentrations (1 vs 2 mM) and temperatures (30, 33, and 37 °C). The trend is that GNP seeds are on average smaller using 2 mM buffer. GNP seed sizes shift from $\approx$ 5 to $\approx$ 10 nm when the preparation temperature is increased from 30−37 °C (Supporting Information Figure S3A−C). The larger seeds, prepared at $\approx$ 37 °C, were used preferentially to grow GNSs. Qualitatively, the separation of LSPR peaks in UV−vis spectra was used to indicate the trend in relative GNS ARs. Greater LSPR peak separation correlates with higher ARs. Thus, Supporting Information Figure S8B−D shows the smallest GNS LSPR peak separations using GNP seeds made in 2 mM buffer. This trend is consistent across seeding volumes (10, 50, and 100 μL).

Crystal sizes and peak dimensions are determined from XRD scans of GNP seeds and GNSs prepared with 10, 50, or 100 μL of seed solution (Table S3, Supporting Information Figure S10). XRD analysis was also helpful to probe preferential orientation of GNS particles. From TEM, the arms of the stars are seen as coplanar. However, enhanced scattering from some crystal orientations may be measured with XRD, indicating preferred crystal orientation. The seeds and GNSs are orientated preferentially in the {111} planes (Table S3). GNSs, however, have a stronger orientation preference, based on {111}/{200} peak height ratios of 2−5 for the GNS versus 1.4 for the seeds. This observation may be interpreted using a simple analogy. Considering the multibranched shapes of these stars, if allowed to dry on a surface, there will be an orientation effect. Statistically, spike tips will align preferentially to the surface. A tetrahedral shape will more likely orientate with two or more branch tips on a surface. The branch edges containing {111} facets directed toward the surface are orientated to the X-ray beam. We hypothesize that the multiple spikes of the GNSs could similarly orient themselves. Chang and co-workers
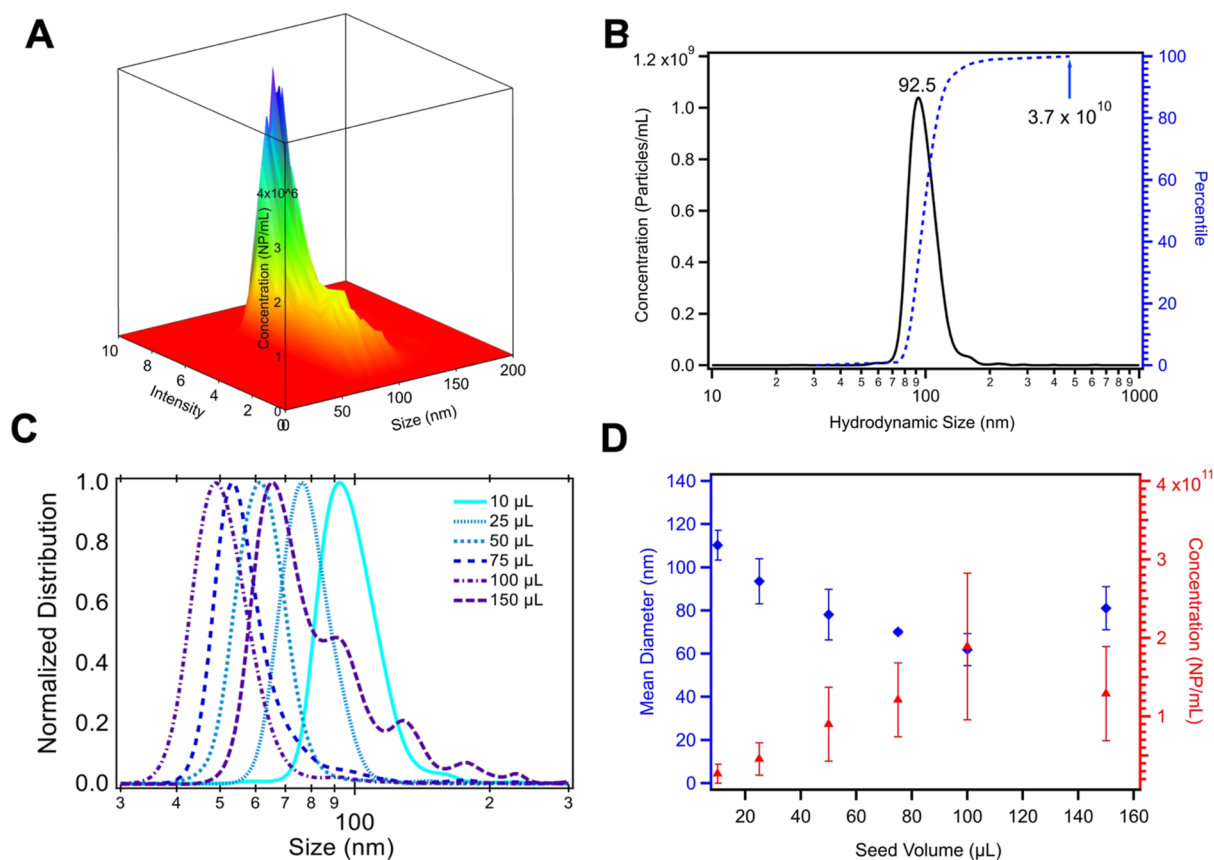
Figure 6. (A) Representative three-dimensional NTA plot of intensity−concentration−size showing GNSs synthesized using 10 μL of GNP seeds. (B) Plot of concentration in particles per milliliter (left, black axis) and percentile (right, blue axis) against hydrodynamic size showing GNSs synthesized using 10 μL of GNP seeds. The peak shown at 92.5 nm is the mode, and the particle total concentration is the integral of the distribution (3.7×10^{10} particles per milliliter) (corrected for dilution factor). (C) NTA distribution plot of normalized concentration against hydrodynamic size of GNSs grown using 10, 25, 50, 75, 100, and 150 μL of GNP seeds. The individual plots represent averages of five independent runs. (D) Plot of GNSs' mean diameter (left, blue axis) and total concentration (right, red axis) against total seed volume (on the 10 mL scale). The error bars represent standard errors taken from three independent experiments.

Table 1. GNS Characterization: Mean and Mode of Sizes, Extinction at 400 nm and at the First Peak, LSPR, and ZP before (CTAB Coating) and after Functionalization with $PEG_{6k}SH$[a]

seed (μL)	mean (nm)	mode (nm)	extinction (400 nm) (M^{-1} cm^{-1})	extinction (first peak) (M^{-1} cm^{-1})	LSPR (nm)	ZP (mV)	ZP with $PEG_{6k}SH$ (mV)
10	110.2 (4.0)	87.6 (3.6)	1.75 (0.23) $\times 10^{10}$	2.71 (0.50) $\times 10^{10}$	639 (9.8)	5	−23
25	93.5 (6.0)	72.7 (2.6)	1.56 (0.41) $\times 10^{10}$	2.47 (0.90) $\times 10^{10}$	613 (5.2)	20	−7
50	78.1 (6.8)	59.5 (1.6)	1.05 (0.33) $\times 10^{10}$	1.52 (0.57) $\times 10^{10}$	587 (2.5)	16	−18
75	70.1 (0.5)	52.0 (1.3)	9.91 (0.49) $\times 10^{9}$	1.4 (0.74) $\times 10^{10}$	577 (6.2)	11	−20
100	61.9 (4.3)	50.2 (0.8)	4.48 (0.79) $\times 10^{9}$	6.82 (1.26) $\times 10^{9}$	567 (6.7)	14	−16
150	81.1 (15.5)	63.4 (9.7)	1.14 (0.43) $\times 10^{10}$	2.08 (0.85) $\times 10^{10}$	561 (4.5)	20	−18

[a]Uncertainties ( ) expressed as standard errors.

interpreted the strong {111} peak in the powder XRD of gold nanotetrapods as being from the dominant crystal face and crystal orientation related to the AR.[37] Additional electron microscopy confirmed that {111} faces are dominant for the tetrapod spikes.

NTA of GNSs. NTA measures NP solution concentrations, diffusion coefficients, and relative intensities (Figure 6A). The integral of the concentration distribution (NP/mL) yields the total NP concentration (Figure 6B). As the TBP GNP seed concentration increases (10−100 μL added), the average hydrodynamic diameter decreases from $\approx$ 100−55 nm (Figure 6C,D). This decrease is consistent with the TEM images, which show that GNSs made using 100 μL of seed solution

have fewer and shorter spikes than those made using 10 μL of seed solution. The corresponding ZPs ranged from +5 to +20 mV, consistent with an efficient CTAB attachment (Table 1). GNSs made with 150 μL of seed solution showed an increase in total size but a decrease in concentration (Figure 6D). The origin of the increase in average particle size and the corresponding decrease in concentration is likely due to particle aggregation with increasing dilution.

Based on DLS intensities, GNSs are distributed in three size populations: < 10, 20−50, and > 100 nm (Supporting Information Figure S11A−F). Sizes are derived from the Stokes−Einstein equation using measured diffusion coefficients, where size is inversely proportional to the diffusion
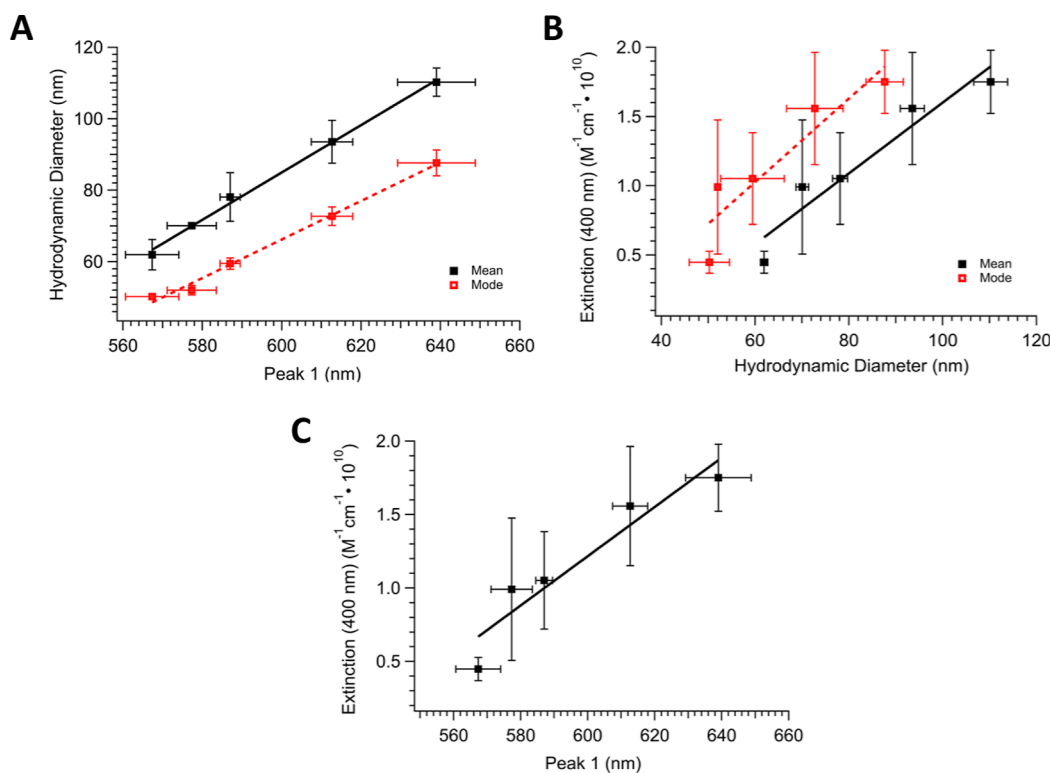
Figure 7. Molar absorption coefficients determined from GNSs seeded with 10−100 μL of GNP seeds. Error bars depict standard errors. This is the average of three independent experiments. (A) Plot of hydrodynamic size (nm) versus wavelength of first (leftmost) peak (nm). Linear regression using eq 2, where $B = 0.66$ and $C = -312.58$ nm for mean and $B = 0.54$ and $C = -257.12$ nm for mode. (B) Plot of molar absorption at 400 nm (M^{-1}cm^{-1}) versus hydrodynamic size (nm). Linear regression using eq 3, where $D = 2.56$ nm^{-1} and $E = -9.55$ for mean and $D = 3.01$ nm^{-1} and $E = -7.82$ for mode. (C) Plot of molar absorption at 400 nm (M^{-1} cm^{-1}) versus wavelength of first (leftmost) peak, where using Equation 4, $F = 1.68$ nm^{-1} and $G = -8.84$.

coefficient. Therefore, the smaller < 10 nm populations are assigned to the higher rotational diffusion coefficients caused by the more rapid tumbling of the spikes relative to that of the overall GNSs. The 20−50 nm populations are assigned to the diffusion contribution of GNS cores.

In Figure 6, the mean hydrodynamic size of GNSs seeded with 150 μL seeds is larger than 100 μL. TEM analysis (Table S1) indicates comparable fractions (15−19% each) of dog-bone, triangle, and webbed morphologies having mean sizes 85, 120, and 100 nm, respectively. Double-terminated NPs of ≈ 170 nm are also present. However, a limitation of TEM analysis is the small sample size (100−200 particles) compared with light scattering analysis (∼ 10^7 to 10^9 particles). Notably, the distribution of GNSs made from the 150 μL seeds is much broader than other distributions, with multiple peaks (Figure 6C). At this seed concentration, the resulting product is very polydisperse. The multiple NP morphologies present are responsible for the skewed and broad hydrodynamic size distribution (Figure 6C). In summary, 150 μL seed volume represents an upper limit for tuning the GNS ARs.

Since absorbance at 400 nm is dominated by interband transitions of metallic gold, molar absorption coefficients (ε_{400}) are estimated using the approach already established for gold nanorods.[59] At this wavelength, the contribution of shape to volume is weak (∼ 10%), so we can use the molar absorption ε_{400} to estimate GNP or GNS concentrations.[16] These calculated molar absorption coefficients are between ∼ 10^9 and 10^{10} M^{-1} cm^{-1}, comparable to previous estimates of ∼ 10^9 M^{-1} cm^{-1}[25,35] (Table 1).

In the UV−vis spectra, two peaks are seen, the first (left, ≈ 550−650 nm) being associated with the dominant core and the second (right, ≈ 600−1100 nm) being associated with the spikes (Figure 5). The first peak is found consistently in the visible range and is therefore utilized for further analysis of hydrodynamic size and molar absorption. The inverse relationship between Au^{3+}/Au(seed) ratio and GNS size contributes added validation for the use of ε_{400} for concentration estimates (Figure 6D). The first peak wavelength is plotted against the hydrodynamic diameter (Figure 7A), and hydrodynamic diameter is plotted against the molar absorption coefficient (Figure 7B). From these data, we were able to plot the first peak values against molar absorption, showing a linear relationship for the GNSs synthesized with 10−100 μL of GNP seeds (Figure 7C). Additionally, this calibration plot is used to estimate molar absorption coefficients at 400 nm and deduce the GNS concentrations based on UV−vis spectra of any batch of prepared GNSs. For example, using eq 5, the concentration of 10 and 100 μL seeded GNSs increases from ≈ 1 × 10^{-5} to ≈ 4 × 10^{-5} μg mL^{-1}, respectively.

An important application of NTA is the investigation of catalytic activity at the solid−liquid interface. In such heterogeneous catalysis systems, reaction rates and corresponding rate constants can be used in concurrence with the concentration and sizes obtained from NTA to derive turnover frequency. This approach is demonstrated with a commonly employed 4-NP reduction model using sodium borohydride and catalysis via GNPs[60] (see Supporting Information). GNSs with different mean ARs were functionalized with PEG-SH (≈

6000 MW). Catalytic effects of PEGylated GNSs were demonstrated using the reduction of 4-NP. There are 10-fold differences in apparent rate constants of GNPs ($\approx$ 1 s^{-1}) versus PEGylated GNSs ($\approx$ 0.1 s^{-1}) in catalyzing the sodium borohydride reduction of 4-NP.

CONCLUSIONS

We demonstrated novel, reproducible synthesis of GNSs by the seed-mediated growth method. Polycrystalline and multiply twinned GNPs ($\approx$ 10 nm) produced using the co-reductants Pluronic F127 and AA served as seeding substrates for GNS synthesis. Strong GNS AR dependencies on pH, ionic strength, and Au^{3+}/Au(seed) concentration ratio are consistent with $V_{dep} \sim V_{diff}$ implying that growth is at least partly under kinetic control. GNS tip-to-core AR was decreased when higher concentrations of gold seeds were added to the growth solution.

To accurately quantify GNP and GNS concentrations, we developed alternative nondestructive, rapid, and quantitative methods based on NTA. NTA can visually track and count heterogeneous NPs within the 30−1000 nm range and estimate concentrations.[9] NTA is a convenient technique (compared to atomic emission) to quantify the concentrations of GNSs for each freshly prepared batch. The heterogeneity of the solutions is accounted for in the analysis. The UV−vis extinction spectra are a superposition of each species. Thus, the derived extinction coefficient will be unique for each batch and will represent solution concentration. NTA for the quantitative characterization of anisotropic NPs could lead to many future applications when combined with other experimental techniques including high throughput methods and advanced mathematical algorithms. Thus, NTA would be valuable in fields such as colloidal catalysis, where varying levels of NP heterogeneity are typical.

ASSOCIATED CONTENT

Ⓢ Supporting Information

The Supporting Information is available free of charge at https://pubs.acs.org/doi/10.1021/acsomega.2c03275.

> TEM, DLS, UV−vis, and XRD characterization of GNP seeds and stars; derivation of the surface-to-volume ratio using Langmuir adsorption isotherms; and additional materials and methods and tables depicting shape distribution and further characterization (PDF)

AUTHOR INFORMATION

Corresponding Author

Christopher C. Perry − *Department of Basic Sciences, School of Medicine, Loma Linda University, Loma Linda, California 92350, United States;* ⓞ orcid.org/0000-0002-4010-9815; Email: chperry@llu.edu

Authors

Natasha T. Le − *Department of Basic Sciences, School of Medicine, Loma Linda University, Loma Linda, California 92350, United States;* ⓞ orcid.org/0000-0003-4258-5302

Timothy J. M. Boskovic − *Department of Basic Sciences, School of Medicine, Loma Linda University, Loma Linda, California 92350, United States*

Marco M. Allard − *Department of Chemistry and Biochemistry, College of Arts and Sciences, La Sierra University, Riverside, California 92505, United States;* ⓞ orcid.org/0000-0002-3005-7230

Kevin E. Nick − *Department of Basic Sciences, School of Medicine, Loma Linda University, Loma Linda, California 92350, United States;* ⓞ orcid.org/0000-0002-8476-1127

So Ran Kwon − *School of Dentistry, Loma Linda University, Loma Linda, California 92350, United States*

Complete contact information is available at: https://pubs.acs.org/10.1021/acsomega.2c03275

Notes

The authors declare no competing financial interest.

REFERENCES

(1) Vo-Dinh, T.; Liu, Y.; Fales, A. M.; Ngo, H.; Wang, H. N.; Register, J. K.; Yuan, H.; Norton, S. J.; Griffin, G. D. SERS nanosensors and nanoreporters: golden opportunities in biomedical applications. *Wiley Interdisc. Rev. Nanomed. Nanobiotechnol.* **2015**, *7*, 17−33.

(2) Yang, L.; Zhou, Z.; Song, J.; Chen, X. Anisotropic nanomaterials for shape-dependent physicochemical and biomedical applications. *Chem. Soc. Rev.* **2019**, *48*, 5140−5176.

(3) Guerrero-Martínez, A.; Barbosa, S.; Pastoriza-Santos, I.; Liz-Marzán, L. M. Nanostars shine bright for you. *Curr. Opin. Colloid Interface Sci.* **2011**, *16*, 118−127.

(4) Perevedentseva, E.; Ali, N.; Lin, Y. C.; Karmenyan, A.; Chang, C. C.; Bibikova, O.; Skovorodkin, I.; Prunskaite-Hyyryläinen, R.; Vainio, S. J.; Kinnunen, M.; et al. Au nanostar nanoparticle as a bio-imaging agent and its detection and visualization in biosystems. *Biomed. Opt. Express* **2020**, *11*, 5872−5885.

(5) Solís, D. M.; Taboada, J. M.; Obelleiro, F.; Liz-Marzán, L. M.; García de Abajo, F. J. Optimization of Nanoparticle-Based SERS Substrates through Large-Scale Realistic Simulations. *ACS Photonics* **2017**, *4*, 329−337.

(6) Bibikova, O.; Haas, J.; López-Lorente, A. I.; Popov, A.; Kinnunen, M.; Meglinski, I.; Mizaikoff, B. Towards enhanced optical sensor performance: SEIRA and SERS with plasmonic nanostars. *Analyst* **2017**, *142*, 951−958.

(7) Daniel, M. C.; Astruc, D. Gold nanoparticles: assembly, supramolecular chemistry, quantum-size-related properties, and applications toward biology, catalysis, and nanotechnology. *Chem. Rev.* **2004**, *104*, 293−346.

(8) Bastús, N. G.; Comenge, J.; Puntes, V. Kinetically Controlled Seeded Growth Synthesis of Citrate-Stabilized Gold Nanoparticles of up to 200 nm: Size Focusing versus Ostwald Ripening. *Langmuir* **2011**, *27*, 11098−11105.

(9) Filipe, V.; Hawe, A.; Jiskoot, W. Critical evaluation of Nanoparticle Tracking Analysis (NTA) by NanoSight for the measurement of nanoparticles and protein aggregates. *Pharm. Res.* **2010**, *27*, 796−810.

(10) Foreman-Ortiz, I. U.; Ma, T. F.; Hoover, B. M.; Wu, M.; Murphy, C. J.; Murphy, R. M.; Pedersen, J. A. Nanoparticle tracking analysis and statistical mixture distribution analysis to quantify nanoparticle-vesicle binding. *J. Colloid Interface Sci.* **2022**, *615*, 50−58.

(11) Mehtala, J. G.; Wei, A. Nanometric resolution in the hydrodynamic size analysis of ligand-stabilized gold nanorods. *Langmuir* **2014**, *30*, 13737−13743.

(12) Arancon, R. A. D.; Lin, S. H. T.; Chen, G.; Lin, C. S. K.; Lai, J.; Xu, G.; Luque, R. Nanoparticle tracking analysis of gold nanomaterials stabilized by various capping agents. *RSC Advances* **2014**, *4*, 17114−17119.

(13) Dragovic, R. A.; Gardiner, C.; Brooks, A. S.; Tannetta, D. S.; Ferguson, D. J.; Hole, P.; Carr, B.; Redman, C. W.; Harris, A. L.; Dobson, P. J.; et al. Sizing and phenotyping of cellular vesicles using Nanoparticle Tracking Analysis. *Nanomedicine* **2011**, *7*, 780−788.

(14) Hoffmann, W. H.; Gao, B.; Mulkerns, N. M. C.; Hinton, A. G.; Hanna, S.; Hall, S. R.; Gersen, H. Determining nanorod dimensions in dispersion with size anisotropy nanoparticle tracking analysis. *Phys. Chem. Chem. Phys.* **2022**, *24*, 13040−13048.

(15) Orendorff, C. J.; Murphy, C. J. Quantitation of metal content in the silver-assisted growth of gold nanorods. *J. Phys. Chem. B* **2006**, *110*, 3990−3994.

(16) Scarabelli, L.; Sánchez-Iglesias, A.; Pérez-Juste, J.; Liz-Marzán, L. M. A "Tips and Tricks" Practical Guide to the Synthesis of Gold Nanorods. *J. Phys. Chem. Lett.* **2015**, *6*, 4270−4279.

(17) Sau, T. K.; Murphy, C. J. Room temperature, high-yield synthesis of multiple shapes of gold nanoparticles in aqueous solution. *J. Am. Chem. Soc.* **2004**, *126*, 8648−8649.

(18) Wu, H.-L.; Chen, C.-H.; Huang, M. H. Seed-Mediated Synthesis of Branched Gold Nanocrystals Derived from the Side Growth of Pentagonal Bipyramids and the Formation of Gold Nanostars. *Chem. Mater.* **2009**, *21*, 110−114.

(19) Sau, T. K.; Rogach, A. L.; Döblinger, M.; Feldmann, J. One-step high-yield aqueous synthesis of size-tunable multispiked gold nanoparticles. *Small* **2011**, *7*, 2188−2194.

(20) Shao, L.; Susha, A. S.; Cheung, L. S.; Sau, T. K.; Rogach, A. L.; Wang, J. Plasmonic properties of single multispiked gold nanostars: correlating modeling with experiments. *Langmuir* **2012**, *28*, 8979−8984.

(21) Xie, J.; Lee, J. Y.; Wang, D. I. C. Seedless, Surfactantless, High-Yield Synthesis of Branched Gold Nanocrystals in HEPES Buffer Solution. *Chem. Mater.* **2007**, *19*, 2823−2830.

(22) Chandra, K.; Culver, K. S. B.; Werner, S. E.; Lee, R. C.; Odom, T. W. Manipulating the Anisotropic Structure of Gold Nanostars using Good's Buffers. *Chem. Mater.* **2016**, *28*, 6763−6769.

(23) Chandra, K.; Kumar, V.; Werner, S. E.; Odom, T. W. Separation of Stabilized MOPS Gold Nanostars by Density Gradient Centrifugation. *ACS Omega* **2017**, *2*, 4878−4884.

(24) Park, K.; Hsiao, M.-S.; Koerner, H.; Jawaid, A.; Che, J.; Vaia, R. A. Optimizing Seed Aging for Single Crystal Gold Nanorod Growth: The Critical Role of Gold Nanocluster Crystal Structure. *J. Phys. Chem. C* **2016**, *120*, 28235−28245.

(25) de Puig, H.; Tam, J. O.; Yen, C. W.; Gehrke, L.; Hamad-Schifferli, K. Extinction Coefficient of Gold Nanostars. *J. Phys. Chem. C* **2015**, *119*, 17408−17415.

(26) Ahmad, N.; Wang, G.; Nelayah, J.; Ricolleau, C.; Alloyeau, D. Exploring the Formation of Symmetric Gold Nanostars by Liquid-Cell Transmission Electron Microscopy. *Nano Lett.* **2017**, *17*, 4194−4201.

(27) Xia, Y.; Xiong, Y.; Lim, B.; Skrabalak, S. E. Shape-controlled synthesis of metal nanocrystals: simple chemistry meets complex physics? *Angew. Chem. Int. Ed.* **2009**, *48*, 60−103.

(28) Carbó-Argibay, E.; Rodríguez-González, B. Controlled Growth of Colloidal Gold Nanoparticles: Single-Crystalline versus Multiply-twinned Particles. *Isr. J. Chem.* **2016**, *56*, 214−226.

(29) Park, S. I.; Song, H. M. Several Shapes of Single Crystalline Gold Nanomaterials Prepared in the Surfactant Mixture of CTAB and Pluronics. *ACS Omega* **2021**, *6*, 3625−3636.

(30) Nehl, C. L.; Liao, H.; Hafner, J. H. Optical properties of star-shaped gold nanoparticles. *Nano Lett.* **2006**, *6*, 683−688.

(31) Sánchez-Iglesias, A.; Winckelmans, N.; Altantzis, T.; Bals, S.; Grzelczak, M.; Liz-Marzán, L. M. High-Yield Seeded Growth of Monodisperse Pentatwinned Gold Nanoparticles through Thermally Induced Seed Twinning. *J. Am. Chem. Soc.* **2017**, *139*, 107−110.

(32) Zhang, X.; Gallagher, R.; He, D.; Chen, G. pH Regulated Synthesis of Monodisperse Penta-Twinned Gold Nanoparticles with High Yield. *Chem. Mater.* **2020**, *32*, 5626−5633.

(33) Zhou, G.; Yang, Y.; Han, S.; Chen, W.; Fu, Y.; Zou, C.; Zhang, L.; Huang, S. Growth of nanobipyramid by using large sized Au decahedra as seeds. *ACS Appl. Mater. Interfaces* **2013**, *5*, 13340−13352.

(34) De Silva Indrasekara, A. S.; Johnson, S. F.; Odion, R. A.; Vo-Dinh, T. Manipulation of the Geometry and Modulation of the Optical Response of Surfactant-Free Gold Nanostars: A Systematic Bottom-Up Synthesis. *ACS Omega* **2018**, *3*, 2202−2210.

(35) Pu, Y.; Zhao, Y.; Zheng, P.; Li, M. Elucidating the Growth Mechanism of Plasmonic Gold Nanostars with Tunable Optical and Photothermal Properties. *Inorg. Chem.* **2018**, *57*, 8599−8607.

(36) Atta, S.; Beetz, M.; Fabris, L. Understanding the role of AgNO3 concentration and seed morphology in the achievement of tunable shape control in gold nanostars. *Nanoscale* **2019**, *11*, 2946−2958.

(37) Chang, Y. X.; Zhang, N. N.; Xing, Y. C.; Zhang, Q.; Oh, A.; Gao, H. M.; Zhu, Y.; Baik, H.; Kim, B.; Yang, Y.; et al. Gold Nanotetrapods with Unique Topological Structure and Ultranarrow Plasmonic Band as Multifunctional Therapeutic Agents. *J. Phys. Chem. Lett.* **2019**, *10*, 4505−4510.

(38) Wang, Y.; He, J.; Liu, C.; Chong, W. H.; Chen, H. Thermodynamics versus kinetics in nanosynthesis. *Angew. Chem. Int. Ed.* **2015**, *54*, 2022−2051.

(39) Xia, Y.; Gilroy, K. D.; Peng, H. C.; Xia, X. Seed-Mediated Growth of Colloidal Metal Nanocrystals. *Angew. Chem. Int. Ed.* **2017**, *56*, 60−95.

(40) Xia, Y.; Xia, X.; Peng, H. C. Shape-Controlled Synthesis of Colloidal Metal Nanocrystals: Thermodynamic versus Kinetic Products. *J. Am. Chem. Soc.* **2015**, *137*, 7947−7966.

(41) Navarro, J. R.; Manchon, D.; Lerouge, F.; Blanchard, N. P.; Marotte, S.; Leverrier, Y.; Marvel, J.; Chaput, F.; Micouin, G.; Gabudean, A. M.; et al. Synthesis of PEGylated gold nanostars and bipyramids for intracellular uptake. *Nanotechnology* **2012**, *23*, 465602.

(42) Fales, A. M.; Yuan, H.; Vo-Dinh, T. Development of Hybrid Silver-Coated Gold Nanostars for Nonaggregated Surface-Enhanced Raman Scattering. *J. Phys. Chem. C* **2014**, *118*, 3708−3715.

(43) Bibikova, O.; Popov, A.; Bykov, A.; Prilepskii, A.; Kinnunen, M.; Kordas, K.; Bogatyrev, V.; Khlebtsov, N.; Vainio, S.; Tuchin, V. Optical properties of plasmon-resonant bare and silica-coated nanostars used for cell imaging. *J. Biomed. Opt.* **2015**, *20*, 76017.

(44) Ngo, V. K. T.; Nguyen, H. P. U.; Huynh, T. P.; Tran, N. N. P.; Lam, Q. V.; Huynh, T. D. Preparation of gold nanoparticles by microwave heating and application of spectroscopy to study conjugate of gold nanoparticles with antibody E. coli O157:H7. *Adv. Nat. Sci. Nanosci. Nanotechnol.* **2015**, *6*, 035015.

(45) Zhang, Z.; Lin, M. Fast loading of PEG−SH on CTAB-protected gold nanorods. *RSC Adv.* **2014**, *4*, 17760−17767.

(46) Ray, D.; Aswal, V. K.; Kohlbrecher, J. Synthesis and characterization of high concentration block copolymer-mediated gold nanoparticles. *Langmuir* **2011**, *27*, 4048−4056.

(47) Sabir, T. S.; Yan, D.; Milligan, J. R.; Aruni, A. W.; Nick, K. E.; Ramon, R. H.; Hughes, J. A.; Chen, Q.; Kurti, R. S.; Perry, C. C. Kinetics of Gold Nanoparticle Formation Facilitated by Triblock Copolymers. *J. Phys. Chem. C* **2012**, *116*, 4431−4441.

(48) Sabir, T. S.; Rowland, L. K.; Milligan, J. R.; Yan, D.; Aruni, A. W.; Chen, Q.; Boskovic, D. S.; Kurti, R. S.; Perry, C. C. Mechanistic investigation of seeded growth in triblock copolymer stabilized gold nanoparticles. *Langmuir* **2013**, *29*, 3903−3911.

(49) Longenberger, L.; Mills, G. Formation of Metal Particles in Aqueous Solutions by Reactions of Metal Complexes with Polymers. *J. Phys. Chem.* **1995**, *99*, 475−478.

(50) Sakai, T.; Alexandridis, P. Mechanism of metal ion reduction, nanoparticle growth and size control in aqueous amphiphilic block

copolymer solutions at ambient conditions. *J. Phys. Chem. B* **2005**, *109*, 7766−7777.

(51) Sakai, T.; Alexandridis, P. Single-Step Synthesis and Stabilization of Metal Nanoparticles in Aqueous Pluronic Block Copolymer Solutions at Ambient Temperature. *Langmuir* **2004**, *20*, 8426−8430.

(52) Haiss, W.; Thanh, N. T.; Aveyard, J.; Fernig, D. G. Determination of size and concentration of gold nanoparticles from UV-vis spectra. *Anal. Chem.* **2007**, *79*, 4215−4221.

(53) Li, C. R.; Lu, N. P.; Xu, Q.; Mei, J.; Dong, W. J.; Fu, J. L.; Cao, Z. X. Decahedral and icosahedral twin crystals of silver: Formation and morphology evolution. *J. Cryst. Growth* **2011**, *319*, 88−95.

(54) Zhang, Q.; Li, W.; Wen, L. P.; Chen, J.; Xia, Y. Facile synthesis of Ag nanocubes of 30 to 70 nm in edge length with CF(3)COOAg as a precursor. *Chemistry* **2010**, *16*, 10234−10239.

(55) van der Hoeven, J. E. S.; Deng, T. S.; Albrecht, W.; Olthof, L. A.; van Huis, M. A.; van Blaaderen, P. E.; van Blaaderen, A. Structural Control over Bimetallic Core-Shell Nanorods for Surface-Enhanced Raman Spectroscopy. *ACS Omega* **2021**, *6*, 7034−7046.

(56) Meena, S. K.; Sulpizi, M. Understanding the microscopic origin of gold nanoparticle anisotropic growth from molecular dynamics simulations. *Langmuir* **2013**, *29*, 14954−14961.

(57) Hao, F.; Nehl, C. L.; Hafner, J. H.; Nordlander, P. Plasmon resonances of a gold nanostar. *Nano Lett.* **2007**, *7*, 729−732.

(58) Wang, H.; Pu, Y.; Shan, B.; Li, M. Combining Experiments and Theoretical Modeling To Interrogate the Anisotropic Growth and Structure-Plasmonic Property Relationships of Gold Nanostars. *Inorg. Chem.* **2019**, *58*, 12457−12466.

(59) Sau, T. K.; Murphy, C. J. Seeded High Yield Synthesis of Short Au Nanorods in Aqueous Solution. *Langmuir* **2004**, *20*, 6414−6420.

(60) Hervés, P.; Pérez-Lorenzo, M.; Liz-Marzán, L. M.; Dzubiella, J.; Lu, Y.; Ballauff, M. Catalysis by metallic nanoparticles in aqueous solution: model reactions. *Chem. Soc. Rev.* **2012**, *41*, 5577−5587.